Chinese Chemical Letters 36 (2025) 109714

Contents lists available at ScienceDirect

Chinese Chemical Letters

journal homepage: www.elsevier.com/locate/cclet

Regulation of uniformity and electric field distribution achieved highly energy storage performance in PVDF-based nanocomposites *via* continuous gradient structure

Jian Wang[a,*], Baohui Wang[a], Pin Ma[a], Yifei Zhang[b], Honghong Gong[c], Biyun Peng[a], Sen Liang[a], Yunchuan Xie[c,*], Hailong Wang[a,*]

[a] Ningxia Key Laboratory of Photovoltaic Materials, School of Materials and New Energy, Ningxia University, Yinchuan 750021, China
[b] Chemistry Department, University of Alberta, Edmonton T6G2N4, Canada
[c] Xi'an Key Laboratory of Sustainable Energy Material Chemistry, School of Chemistry, Xi'an Jiaotong University, Xi'an 710049, China

ARTICLE INFO

Article history:
Received 24 January 2024
Revised 27 February 2024
Accepted 1 March 2024
Available online 7 March 2024

Keywords:
Nanocomposites
Nanofibers
PVDF-based polymers
Breakdown strength
Energy storage

ABSTRACT

PVDF-based nanocomposites have gained significant focus in capacitors for their excellent dielectric strength, its multi-scale structural inhomogeneity is the bottleneck for improving the energy storage performance. Here, the composite components are optimized by the matrix modification, BST ($Ba_{0.6}Sr_{0.4}TiO_3$) ceramic fibrillation and surface coating. A series of PVDF/polymethyl methacrylate/lysozyme@BST nanofibers with continuous gradient distribution (PF-M/*m*BST nf-g) are prepared by the concentration gradient-biaxial high-speed electrospinning. The finite element simulation and experiment results indicate that the continuous gradient structure is favorable for the microstructure and inhomogeneity of the electric field distribution, significantly increasing the breakdown strength (E_b) and the permittivity (ε_r), as well as effectively suppressing the interfacial injected charge and leakage current. As a result, the energy storage density (U_e) of 23.1 J/cm^3 at 600 MV/m with the charge-discharge efficiency (η) of 71% is achieved compared to PF-M (5.6 J/cm^3@350 MV/m, 65%). The exciting energy storage performance based on the well-designed PF-M/*m*BST nf-g provides important information for the development and application of polymer nanocomposite dielectrics.

Film capacitors are widely used in electronic power systems such as hybrid vehicles, photovoltaic/wind inverters and electromagnetic ejection systems, compared to energy storage sources like supercapacitors and chemical batteries, it has fast charging-discharging speed (<1 ms) and high-power density (~10^8 W/kg) characteristics [1–6]. Generally, the current common polymer dielectrics, such as polypropylene, polyphenylene sulfide, polystyrene and polyester, have the disadvantage of low energy storage density (U_e) due to the low ε_r limitation [7]. For example, the U_e of most widely used biaxially oriented polypropylene (BOPP) film is still only 2–3 J/m^3 at 600 MV/m electric field (E). Therefore, a large volume (~25%) is required to compensate for the shortcomings of energy deficiency [8,9], which is far from meeting the design needs of advanced electronic power equipment for severe light-weighting and integration.

According to the dielectric energy storage density equation $U_e = 0.5\varepsilon_r\varepsilon_0 E_b^2$ (Fig. S1 in Supporting information), the high U_e requires high ε_r and E_b. Theoretically, polymer/ceramic composites combine the characteristics of flexible polymers with high E_b and ceramics with high ε_r [10,11]. The addition of high ε_r (~10^3) ceramic fillers such as barium titanate ($BaTiO_3$), lead zirconate titanate (PZT) and calcium copper titanate (CCTO) to the polymer matrix can yield nearly 100 ε_r, which is near to its overpermeability theoretical quotient [12–14]. However, excessive differences at the polymer/ceramic interface are prone to electric field distortion. Besides, the high filler content required to exceed the theoretical quotient of percolation exacerbates the leakage current intensity, leading to a sudden drop in E_b and U_e.

Usually, the direct enhancement of ε_r tends to cause a decrease in E_b. Optimizing the polymer matrix, ceramic fillers and interface is the effective way to enhance U_e [15–17]. Zhang *et al.* introduced homopolymers such as polymethyl methacrylate (PMMA) and polystyrene into PVDF for modulating the crystalline shape and reduce the ferroelectric relaxation energy loss, improving the η 107% with the enhancement of E_b by 20% [18–20]. Composite in-

* Corresponding authors.
E-mail addresses: wangjian@nxu.edu.cn (J. Wang), ycxie@xjtu.edu.cn (Y. Xie), wanghailong@nxu.edu.cn (H. Wang).

https://doi.org/10.1016/j.cclet.2024.109714
1001-8417/

terface is an essential factor affecting their dielectric energy storage properties. The organic or inorganic transition layer could improve interfacial compatibility and mitigate *E* distortion, enhancing ε_r while maintaining a high E_b, ultimately increasing U_e to 10–20 J/cm^3 [21–24]. Besides, the ceramic fillers structure can modulate the *E* distribution inside the composites and thus affect its E_b. It is found that the 1D/2D ceramic particles with high aspect ratio can effectively E_b. Moreover, the multilayer film structure such as sandwich, interlayer and multi-nanoparticle film can achieve the controlled distribution of *E* in the composites to mitigate *E* distortion and leakage current, while the interlayer barrier effectively suppresses carrier migration, thus increasing E_b [25–28].

The existence of amorphous regions, filler agglomerates, and physical defects in polymer composites disrupts the continuity of their multiscale structures, which are major factors contributing to the decreased dielectric energy storage performance of composites. To address this issue, we devised a strategy for fabricating composite films with a continuous gradient structure. Specifically, we first prepared a relaxed P(VDF-HFP)/PMMA (PF-M) matrix through aggregation state structure modulation. Next, *m*BST nf was synthesized using high-speed electrospinning and lysozyme self-assembly techniques. Then employed continuous electrospinning and heat treatment methods to regulate the orientation and spatial distribution of *m*BST nf, the continuous gradient structure effectively minimized multiscale structure differences within the composite and promotes the uniform distribution of *E*, and finally obtain the continuous gradient film PF-M/*m*BST nf-g with excellent energy storage performance.

Chemicals and materials: Solvay Solexis provided the P(VDF-HFP) (99%, 100M, VDF/HFP = 80/20 mol%), PMMA (99%, 60M) was derived from Aladdin Reagent (Shanghai) Co., Ltd. Sinopharm Group Chemical Reagent Co., Ltd. offered barium acetate ($Ba(CH_3COO)_2$) and strontium acetate ($Sr(CH_3COO)_2$) (99.99%, Xi'an city, China). Tetrabutyl titanate, acetylacetone ($C_5H_8O_2$), aceticacid (CH_3COOH), anhydrous ethanol and *N*,*N*-dimethyl formamide (DMF) were all provided by Tianjin Chemical Reagents Co., Ltd. Lysozyme (99%, derived from egg white), TCEP (99% HPLC) and 4-(2-hydroxyethyl)−1-piperazineethanesulfonic acid (HEPES, pH 7.2-7.4, drybasis, 99%) were purchased from Shanghai Yuanye Biotechnology Co., Ltd. (Shanghai, China). The polymers are subjected to an acetone dissolution-deionized water 3 times before use to remove impurities.

Preparation of BST Nanofibers and *m*BST nf: The preparation of BST precursor solution, BST nanoparticles, and lysozyme modification of filler surfaces follows our previous work [29], 20 mL of BST precursor solution was taken and the concentration was adjusted by adding 1 mL of anhydrous ethanol to prepare the electrospinning precursor solution, which was placed in a syringe with a 20-gauge metal needle, and the applied DC voltage was set at 20 kV, the distance between the metal needle and the receiving drum is 15 cm, the syringe advance speed is 0.2 mm/min and the receiving drum rotation speed is 150 rpm. Set the temperature inside the electrospinning machine at 25 °C and humidity below 20%. Then the BST electrospinning film is carefully scraped and calcined in a muffle furnace at 800 °C for 4 h to obtain white BST powder, which is BST nanofiber (BST nf). In order to improve the weak interface between polymer/ceramic, the surface modification of BST nf by lysozyme was used to successfully prepare a core-shell structure PTL@BST nf enriched with polar groups such as -COOH, -OH, -NH_2 and -SH on the surface, denoted as *m*BST, *m*BST nf.

Preparation of nanocomposite films: Based on our previous work, a blended polymer with 20 wt% PMMA content was selected as the matrix. Biaxial electrospinning with a gradual change in the advancement speed of the precursor solution was employed to fabricate the composites with a continuous gradient distribution of fillers, and the advancement speeds of the PF-M solution and the PF-M/*m*BST nf solution are shown in Fig. 1. To ensure that the *m*BST nf could be oriented, a high-speed receiver with 2000 rpm was selected. A continuous gradient composite film with *m*BST nf content tapering from the middle of the film to the outside was prepared by hot pressing and quenching. To compare the effects of nanofibrous ceramics and continuous gradient structures, PF-M/*m*BST-r with uniform distribution of *m*BST, PF-M/*m*BST nf-r with uniform distribution of *m*BST nf were prepared following a similar approach.

Characterization: The Fourier transform infrared (FTIR) spectra were measured in transmission mode on a Spectrum Two (PerkinElmer, USA). X-ray diffraction (XRD) was carried out on a D/max 2200 PC (Rigaku Corporation, Japan) to obtain the crystal structure information of sample with the X-ray wavelength of 1.542 Å (Cu Kα radiation, 40 kV and 0.1 A). The mechanical properties of the film samples were characterized by dynamic mechanical analysis (DMA) using a universal electronic tensile tester (STM-1, 100 N load cell, Shanghai Stroma, China), The morphology of BST and *m*BST was obtained by using transmission electron microscopy (TEM, JEM-200CX, Japan). The microscopic appearance of nanocomposites was observed with a field-emission scanning electron microscopy (FE-SEM, JSM-7500F, JEOL, Japan), and the films were fragmented with liquid nitrogen and splashed with a layer of thin gold before observing. The E_b of nanocomposites was evaluated by the Dielectric Withstand Voltage Test (DW-P504–4ACD2, Tianjin Dongwen, China) according to ASTM D149 under a 0.3 kV/s DC voltage ramp. Dielectric properties of all nanocomposites were collected in the frequency series from 1 Hz to 1 MHz *via* a Novocontrol Concept 80 (Germany). High-field *D*-*E* loops were obtained using the ferroelectric test system (HUACE 2000, Beijing huace, China), where the films were exposed to a triangular unipolar wave with a 10 Hz frequency.

Phase-field simulations: For the phase field simulation of the nanocomposites, the spatial distribution of the *E* in steady-state system under the 2D AC/DC module is modeled; for the dynamic breakdown process, the scalar phase field $s(x, t)$ is introduced using a modified phase-field model to describe it. As detailed in Supporting information, an electric dendritic channel grows when the electrostatic energy released per unit exceeds the energy required for breakdown, causing the dielectric breakdown velocity to be proportional to the energy driving force. In this case, the fixed dielectric constant ($\varepsilon(d)$) of the dielectrics can be defined as Eq. 1:

$$\varepsilon(d) = \frac{\varepsilon^0}{f(s) + \eta} = \frac{\varepsilon^0}{4s^3 - 3s^4 + \eta} \quad (1)$$

the ε_r values of the PF-M matrix and BST nanofillers were taken as 9.9 and 1800, respectively, which was fitted from the experimental measurements on the pure BST sample at 100 Hz. Neglecting polymer/filler interface defects.

Fig. 1a depicts the successful surface modification of *m*BST nf with PTL as described in the Methods section, the illustration shows that a fibrous and uniformly coated PTL surface is present in BST nf. As shown in Fig. 1b and its illustration, to address the inhomogeneity of nanocomposites, this work focuses on three aspects for the polymer matrix components, two-phase compatibility and composite structure: (1) The PVDF crystalline/amorphous phase difference was eliminated by using the low energy loss PF-M all-organic hybrid polymer matrix as Figs. S2 and S3 (Supporting information); (2) The BST nf was encapsulated by using lysozyme enriched in -OH and -NH_2 to enhance the two-phase compatibility; (3) For the BST nf oriented and continuous gradient-distributed films (PF-M/*m*BST nf-g3 (3 vol%)), a high-speed electrospinning-hot pressing process was used while controlling the speed of the PF-M and PF-M/*m*BST nf precursor solutions. High-quality composite films were produced through quenching processes. For highlighting the effect of continuous gradient distribution of BST nf, as shown

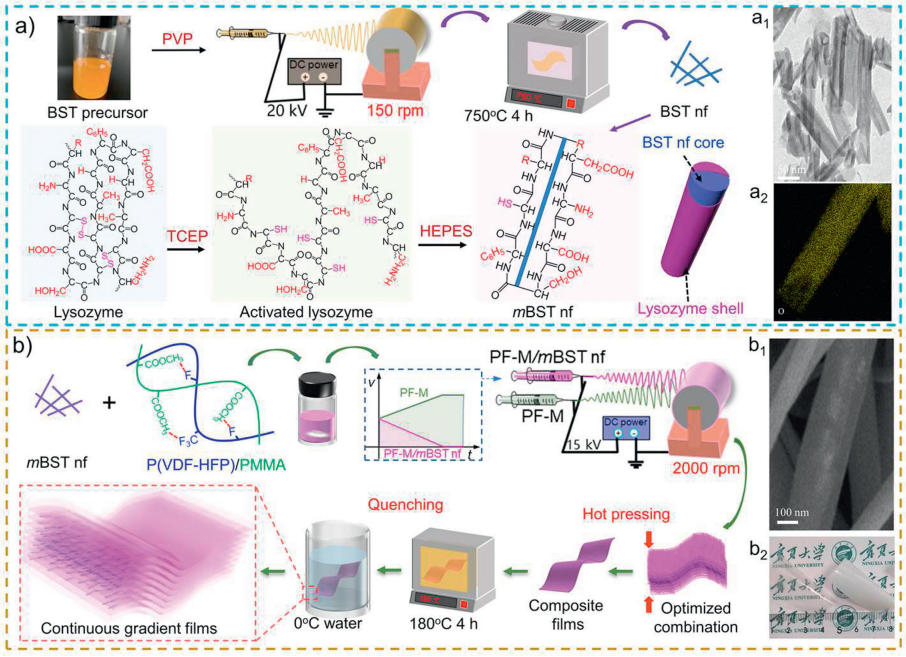

Fig. 1. (a) Preparation of BST nf by electrospinning and its surface self-assembly for growth of lysozyme ((a_1) TEM of *m*BST and (a_2) its O-element distribution). (b) Preparation of PF-M/*m*BST nf continuous gradient nanocomposite dielectric films by electrospinning-hot pressing process ((b_1) SEM of composite fibers, (b_2) optical photographs of PF-M and PF-M/*m*BST nf-g3 films).

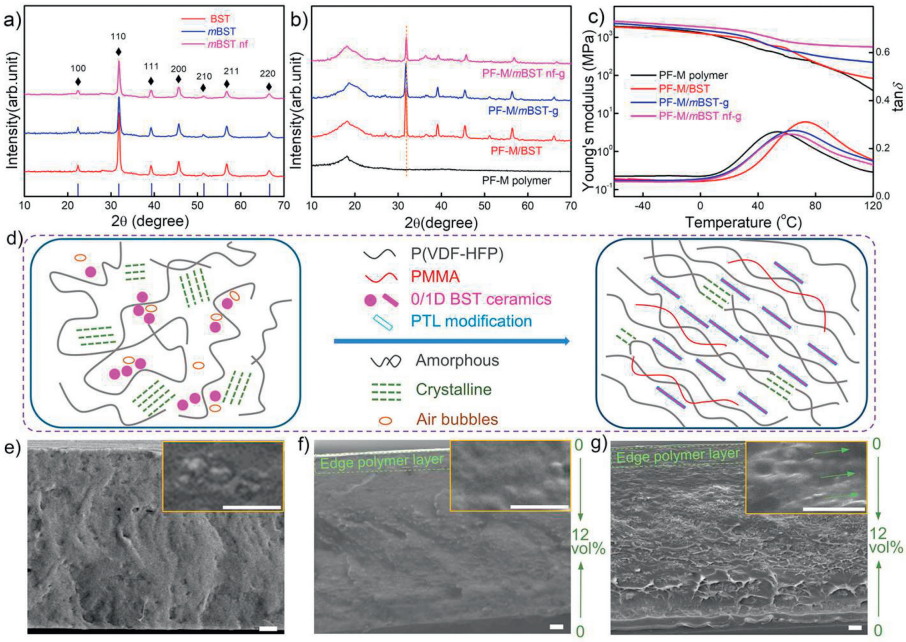

Fig. 2. Comparison of XRD patterns of (a) different ceramics and (b) their nanocomposites, (c) DMA curves of nanocomposites. (d) Schematic diagram of interactions between polymer matrix and fillers. SEM images of (e) PF-M/BST, (f) PF-M/*m*BST-g and (g) PF-M/*m*BST nf-g (all scale is 1 μm).

in Fig. S4 and Table S1 (Supporting information), BST fillers and their composites were prepared according to similar methods.

Fig. 2a and Fig. S5a (Supporting information) presents the XRD and FT-IR results of three nanoparticles. The absorption bands detected at 1042 cm^{-1}, 1610 cm^{-1}, and 3446 cm^{-1} in *m*BST are primarily assigned to the bending vibrations of the -NH_2, -N-H-, and -OH bonds of the protein in lysozyme, respectively [30,31]. Apparently, all the XRD analysis revealed seven characteristic diffraction peaks at $2\theta = 22.2°$, 31.7°, 39.2°, 45.5°, 51.3°, 56.6°, and 66.6°, corresponding to the (100), (110), (111), (200), (210), (211), and (220) peaks of BST with an inclusion crystal structure (JCPDS No. 34–0411) [29,32]. The crystal structures of BST, *m*BST and untreated *m*BST nf samples remain unchanged according to the XRD results. As depicted in Fig. 2b, the pristine PF-M shows an amorphous structure with no distinct XRD diffraction peaks, but a broad diffusion peak at about $2\theta = 17.8°$, and the incorporation of BST, *m*BST, or *m*BST nf does not influence the chain conformation or crystal structure of the PF-M matrix (Fig. S5b in Supporting information). The thermo-mechanical relationships of the films in Fig. 2c demonstrate that the addition of BST, *m*BST or *m*BST nf has little effect on the Young's modulus at room and low temperatures, which is consistent with the stress-strain relationship in Fig. S6

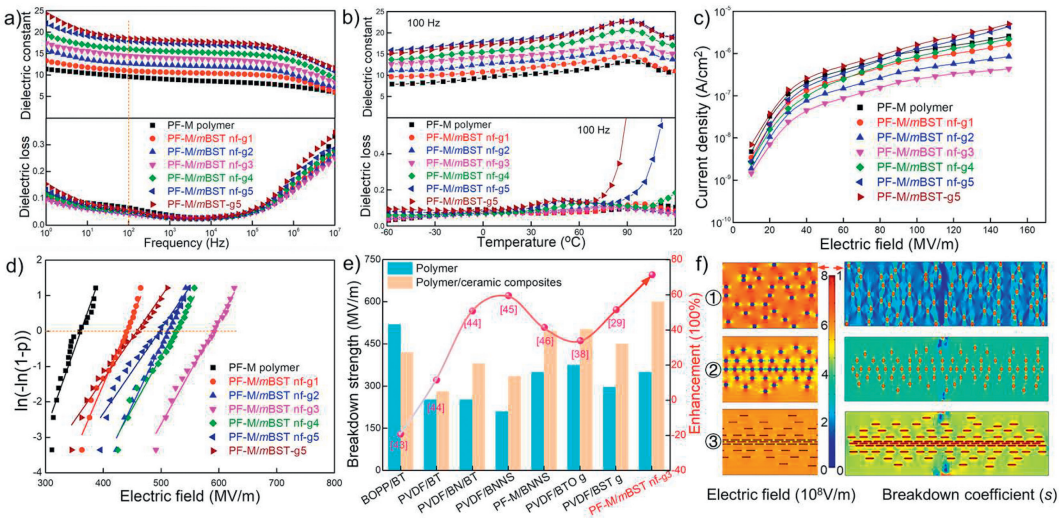

Fig. 3. The ε_r and tanδ of nanocomposite films as a function of (a) frequency or (b) temperature at 100 Hz. (c) Leakage current density and (d) Weibull distribution of measured E_b, as a function of the E of nanocomposite films. (e) Comparison of the enhancement of E_b of polymer matrix by different ceramic fillers. (f) Phase field simulation and breakdown path simulation of different nanocomposite (1. PF-M/*m*BST-r, 2. PF-M/*m*BST-g, 3. PF-M/*m*BST nf-g, dark blue color represents the breakdown path with s close to 0).

(Supporting information). However, at high temperatures, the addition of *m*BST nf with a high aspect ratio significantly enhances the thermo-mechanical properties of the polymer [33,34]. This enhancement is attributed to the orientation of *m*BST nf and the gradient distribution, which effectively reduces the structural defects in the nanocomposites (Fig. 2d). Additionally, the homogeneous composite structure effectively strengthens the linkage between the multiscale components of the nanocomposites.

Fig. 1b and Figs. S7a and b (Supporting information) demonstrate that the addition of *m*BST nf or *m*BST into PF-M fibers through electrospinning results in a uniform dispersion. Benefiting from the high-speed electrospinning technique to control the gradient concentration and orientation of *m*BST nf, nanocomposite films with a continuous gradient distribution and fiber orientation can be fabricated as shown in Figs. 2e-g and Figs. S7c and d (Supporting information). Compared to the dispersion of BST, the *m*BST nf are uniformly embedded and oriented in the PF-M matrix, thus the nanocomposites without noticeable gaps or interfacial defects. This suggests a strong and compatible interfacial bonding between the polymer matrix and the nanofillers, likely due to the PTL surface modification [32]. Additionally, the nanocomposite films had a precisely controlled continuous gradient distribution of *m*BST nf and no obvious interfacial abruptness in the longitudinal direction, which is consistent with the biological gradient structure [35]. Fig. 2g shown the presence of a submicron polymer buffer layer at the edge of PF-M/*m*BST nf-g3, which reduces the influence of the electrode on the *m*BST nf, thereby slowing down the formation of the conductive path.

Fig. 3a illustrated that the ε_r values of the nanocomposites were decreasing with increasing frequency, which was quite comparable to the trend of the PF-M matrix [36]. It is interesting to observe that ε_r is almost irrelevant to the distribution of *m*BST nf, and the ε_r of the three nanocomposite films are very close to each other. ε_r is the vector sum of all polarizations along the direction of the E, which is independent of the distribution of *m*BST nf in the nanocomposite film [36,37]. The addition of *m*BST nf with high ε_r resulted in higher ε_r for all nanocomposite films compared to the PF-M matrix. For instance, the ε_r of PF-M/*m*BST nf-g3 reached 14.8 (10^2 Hz), which is almost 50% higher than that of the PF-M matrix (ε_r ~9.9@10^2 Hz). Additionally, the tanδ of the dielectrics based on polymers is primarily attributed to its ionic conductivity and interfacial polarization at low frequencies (~10^2 Hz). The moderate amount of *m*BST nf traps the charge, and the outer polymer of the gradient film inhibits charge injection [38], so that the PF-M/*m*BST nf-g3 demonstrates low tanδ and conductivity in Fig. S8 (Supporting information). The relationship between ε_r and temperature for dielectrics at 10^2 Hz, confirms the trend of increasing ε_r with *m*BST nf loading content in Fig. 3b. It is worth noting that the tanδ of the composites is lower than that of the PF-M matrix at lower temperatures (60 °C). However, as the temperature increases, the tanδ becomes significantly higher than the PF-M. The instability of PVDF-based polymers at high temperatures can cause polarization loss between the free filler/polymer, resulting in the observed behavior [39,40]. Nevertheless, PF-M/*m*BST nf-g3 maintained a tanδ below 0.05 even at 120 °C, indicating stability of the dielectric properties.

From the relationship of U_e, it can be seen that another major element affecting the U_e is E_b, it is commonly recognized that E_b in dielectric films is intimately related to the conductance associated with the E. Fig. 3c shows that the current density in the measured dielectrics decreases significantly by an order of magnitude with the introduction of *m*BST nf. For instance, 3.1×10^{-6} A/cm^2 for PF-M decreases to 4.3×10^{-7} A/cm^2 for PF-M/*m*BST nf-g3 at 150 MV/m. It is observed that when the E exceeds 100 MV/m, the leakage current density in PF-M/*m*BST nf-g becomes flatter with increasing E, indicating that a dielectric with a continuous gradient structure favors charge transfer in high E. Predictably PF-M/*m*BST nf-g3 has the highest E_b, and the two-parameter Weibull distribution function is commonly utilized to measure the E_b in Fig. 3d and Fig. S9 (Supporting information) by Eq. 2:

$$F(x) = 1 - \exp\left[-\left(\frac{x}{\alpha}\right)^{\beta}\right] \quad (2)$$

where F(x) is the cumulative probability of electrical breakdown, x is the measured value of E_b, α is the scale parameter of the E, and the E of a sample with a breakdown probability of 63.2% is E_b. Additionally, the shape parameter β indicates the scattering of the data, with higher values implying greater reliability of the surface data [41,42]. It is evident that the α-values for PF-M and PF-M/*m*BST nf-g3 are measured at 348 MV/m and 600 MV/m in Fig. S10 (Supporting information). The elevated E_b-value in PF-M/*m*BST nf-g can be attributed to the improved Young's modulus (Y), as supported by the Stark-Garton model equation (Eq. 3),

commonly followed by numerous ferroelectric polymers [13].

$$E_b = 0.6 \times (Y/\varepsilon_0\varepsilon_r)^{0.5} \quad (3)$$

As a result, the Y exhibits an increase from 0.57 GPa for PF-M to 2.33 GPa for PF-M/*m*BST nf-g3. This enhanced modulus effectively counteracts deformation induced by coulombic stresses in high E, thereby ensuring the film's mechanical stability and electrical insulation are adequately maintained. However, as the *m*BST nf content exceeded 4 vol%, a noticeable decrease in the E_b value of PF-M/*m*BST nf-g was observed. This finding suggests that an excessive amount of *m*BST nf content could lead to agglomeration and the formation of interfacial defects in Fig. S11 and Table S2 (Supporting information). The continuous gradient distribution of *m*BST nf in the composites exerts a key role in effectively reducing its inhomogeneity, this unique characteristic of *m*BST nf leads to a significant enhancement in the E_b value compared to that of conventional polymer composite dielectrics in Fig. 3e [29,38,43-46].

To emphasize the significance of the continuous gradient distribution of BST, we conducted finite element simulations using COMSOL Multiphysics. Fig. 3f and Fig. S12 (Supporting information) illustrates the E and leakage current in nanocomposite films with three distinct nanofiller distribution. The E of dielectrics is inversely proportional to its ε_r, therefore an uneven distribution of the E arises in the nanocomposites, particularly in the vicinity of the fillers [47]. The gradient structure exhibits a smaller E then others, which due to the middle layer of films bears low E and weakens the electric field distortion, while the pure polymer layer at the electrodes is also effective in suppressing the injected charge and leakage current (Fig. S13 in Supporting information). Additionally, the film's dielectric properties continuously change in the electric field, creating an energy barrier that effectively inhibits the growth of electric trees and leads to a higher E_b [29].

The breakdown phenomenon in dielectrics is characterized by its rapid and transient nature. To gain clearer insights into the impact of structures on E_b, an optimized phase field model is employed to simulate the dynamic breakdown process. In COMSOL, the dynamic breakdown parameters are precisely defined, when the electrostatic energy released per unit exceeds the energy threshold for breakdown, an electrical dendritic channel forms, leading to a dielectric breakdown rate directly proportional to the energy driving force. To further characterize this process, a scalar phase field, denoted as s(x, t), is introduced and can be mathematically defined by Eqs. 4 and 5 [48].

$$\frac{\partial}{\partial \overline{x_i}}\left[\frac{1}{f(s)+\eta}\cdot\frac{\partial \overline{\phi}}{\partial \overline{x_i}}\right] = 0 \quad (4)$$

$$\frac{\partial s}{\partial \overline{t}} = f'(s) + \frac{\partial^2 s}{2\partial \overline{x_i}\partial \overline{x_i}} - \frac{f'(s)}{2[f(s)+\eta]^2}\cdot\frac{\partial \overline{\phi}}{\partial \overline{x_i}}\cdot\frac{\partial \overline{\phi}}{\partial \overline{x_i}} \quad (5)$$

where the former is the dimensionless form of Euler's equation and the latter is the dielectric breakdown field variable in the E. Based on these, the damage variable s is color-coded to represent its size, with $s = 1$ denoting the intact state and $s = 0$ indicating dielectric breakdown. It is worth noting that a higher s corresponds to greater material stability. Consequently, the breakdown path within the dielectrics can be analyzed by observing the growth path highlighted in dark blue. The breakdown path of the PF-M near the electrode exhibits slower growth along the E direction in PF-M/*m*BST nf-g3. More importantly, the breakdown path traversing the nanofiber fillers region with an increasing mass fraction prompts the movement of free electrons within the Debye length of the nanoparticles [49]. These electrons experience dispersion or attraction, resulting in energy dissipation and a slow breakdown process in PF-M/*m*BST nf-g. This behavior signifies their heightened insulation strength, further supported by consistent experimental results.

Fig. 4a and Fig. S14 (Supporting information) presents the electric displacement-electric field (D-E) loops of the dielectrics at progressively enhanced E, as well as a comparison of their residual/maximum polarization (P_r/P_m) at 300 MV/m is displayed in Fig. 4b. P_m is positively proportional to the addition of high-ε_r *m*BST nf, while the suppression of P_r may be ascribed to the moderate amount of nanofiber-reinforced composites amorphous region modulus, limiting the polymer ferroelectric domains flip and thus reducing P_r. At an E_b of 350 MV/m, the PF-M polymer has an U_e of 5.6 J/cm^3 and a η of 65%, which is a significant enhancement compared to PF-M matrix in Fig. 4c. Due to the more significant P_r/P_m difference, the U_e of PF-M/*m*BST nf-g3 can reach as high as 23.1 J/cm^3. More excitingly, it can maintain 71% of η at a high E_b of 600 MV/m, this is 412.5%, 111%, and 171.4% of PF-M matrix in Fig. 4d, respectively, which is undoubtedly exciting news for the application of PVDF-based composite dielectrics.

Fast discharge performance is an essential property of energy storage capacitors, the discharge curve of PF-M/*m*BST nf-g3 is compared with that of the BOPP in Fig. 4e and Fig. S15 (Supporting information), and the schematic diagram of the test circuit is presented in Fig. 4f. Note that the discharge time of the dielectrics is when the discharge density reaches 90% of the total discharge density. The analysis shows that the PF-M/*m*BST nf-g3 has a very short discharge time of 7.09 μs, which is shorter than that of BOPP (13.1 μs). Meanwhile, the charge-discharge stability of the dielectric films was also investigated. Fig. 4g shows U_e and η at 300 MV/m of PF-M/*m*BST nf-g3 subjected to 1000 charge-discharge cycles, and it can be seen that there is no obvious fluctuation in the data, indicating that it has a high reliability. The improved charge-discharge performance can be attributed to the continuous gradient structure harmonizing the electrical properties of the nanocomposite. When comparing the energy storage performance of different dielectrics (including normal polymers, modified polymers, hybrid polymers, ceramics and polymer/ceramic composites) in Fig. 4h, PF-M/*m*BST nf-g3 nanocomposite films with a continuous gradient structure exhibit a significant advantage, providing a basis for improving the performance of PVDF-based dielectrics [50–59].

To elucidate the mechanism of our work (polymer matrix modification, filler design and surface modification, filler distribution and continuous gradient structure) to enhance the capacitive properties, we compared the dielectric-ferroelectric-energy storage properties of a series of dielectrics, as shown in Fig. 5 and Fig. S16 (Supporting information). On the one hand, the PTL-modified BST nf remarkably improves the two-phase compatibility of the composites; on the other hand, the continuous gradient and orientation distribution of the nanofiber filler acts as a large-area physical barrier and suppresses carrier migration, prolonging the growth process of the breakdown paths, which leads to the enhancement of the E_b and the decrease of the dielectric loss. Through meticulous attention to chemical composition and structural design, it is evident that sample PF-M/*m*BST nf-g exhibits a notable advantage over the other samples. This finding serves as further validation of the significant contribution of *m*BST nf in enhancing the dielectric properties of PVDF-based nanocomposites.

In summary, our study successfully fabricates a nanocomposites film with significantly enhanced electrical properties through chemical modification and continuous gradient structure design. The incorporation of *m*BST nf effectively mitigates interfacial defects and improves the dielectric strength and Young's modulus. Moreover, the continuous gradient and orientation distribution of nanofibers effectively suppresses carrier migration and leakage current. These combined effects synergistically enhance the E_b and ε_r, while reducing conduction loss under high E. Notably, the PF-M/*m*BST nf-g3 demonstrates exceptional energy storage performance, with a U_e of 23.1 J/cm^3 and a η value exceeding 71% at

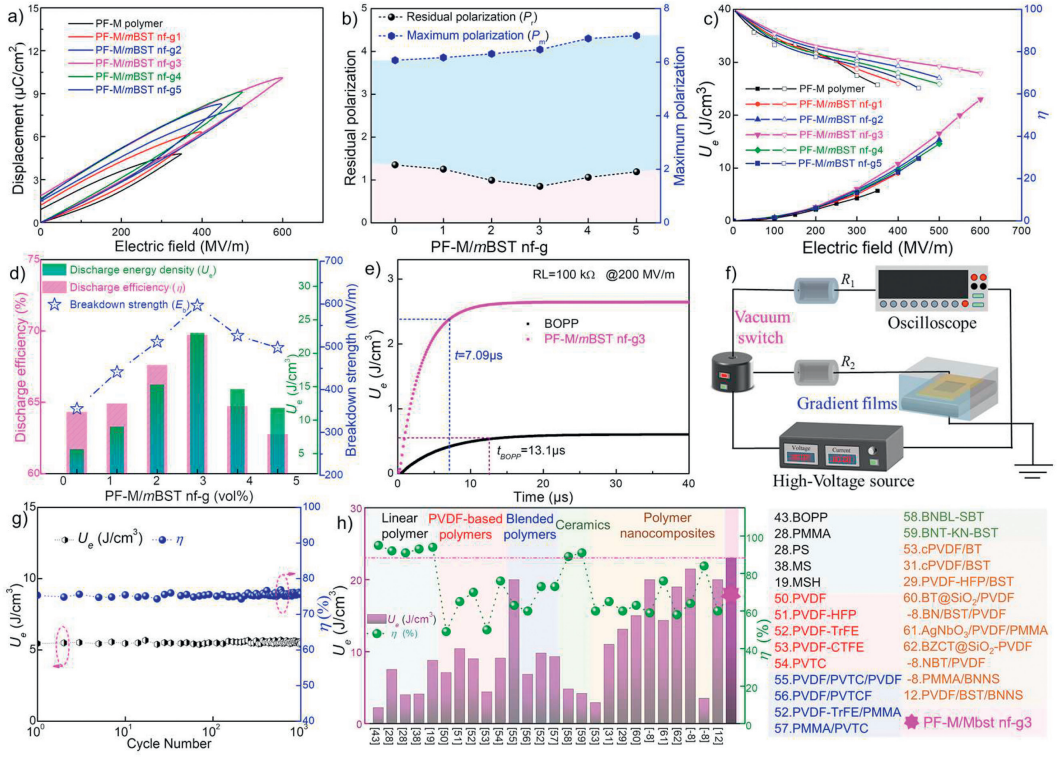

Fig. 4. PF-M/*m*BST nf-g films with (a) *D-E* loop, (b) P_r/P_m comparison at 300 MV/m. (c) U_e and η, and (d) electrical properties comparison, as a function of different *m*BST nf contents. (e) Discharge rate and (f) its test schematic. (g) Charge/discharge cycling stability of PF-M/*m*BST nf-g3 nanocomposites. (h) Comparison of energy storage performance of common dielectrics in recent years.

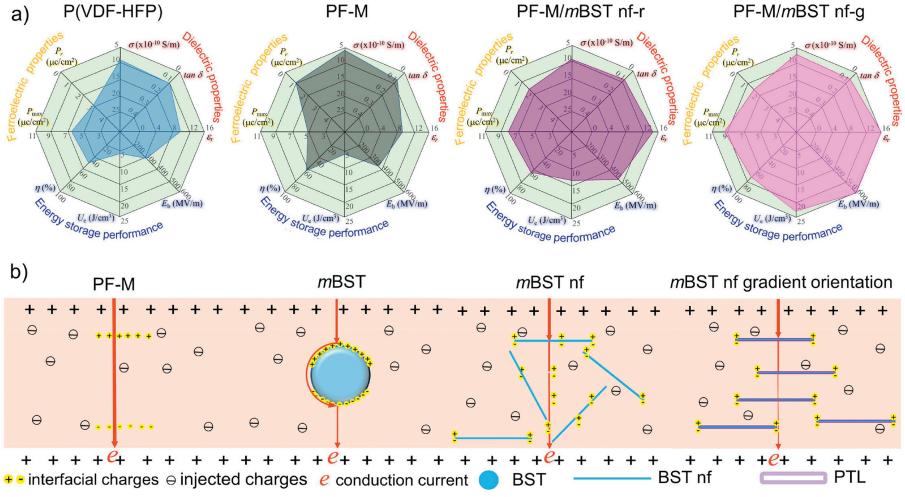

Fig. 5. (a) Dielectric and capacitive parameters of P(VDF-HFP), PF-M, PF-M/*m*BST nf-r, PF-M/*m*BST nf-g continuous gradient nanocomposites, and (b) schematic diagram of breakdown mechanism.

600 MV/m. Additionally, it exhibits ultrafast discharging rates and stable charge-discharge cycling performance. This study presents a well-designed continuous gradient structure that significantly enhances the energy storage performance of polymer nanocomposite dielectrics, and hold great promise for future advancements in the field.

Declaration of comepting interest

The authors declare that they have no known competing financial interests or personal relationships that could have appeared to influence the work reported in this paper.

Acknowledgments

The authors are grateful for the support and funding from the National Natural Science Foundation of China (Nos. 51773164, 5186020071) and Ningxia Natural Science Foundation (No. 2023AAC03104). We would like to thank Analysis and Testing Center of Ningxia University for their assistance with SEM and TEM analysis.

Supplementary materials

Supplementary material associated with this article can be found, in the online version, at doi:10.1016/j.cclet.2024.109714.

References

[1] Z. Guo, X. Han, C. Zhang, et al., Chin. Chem. Lett. 35 (2024) 109007.
[2] S. Zhang, H. Chen, Y. Xu, et al., Rare Metals 41 (2022) 3129–3141.
[3] G. Zeng, Y. Wang, X. Lou, et al., J. Energy Storage 77 (2024) 109859.
[4] W. Deng, Y. Li, D. Xu, et al., Rare Metals 41 (2022) 3432–3445.
[5] X. Wen, J. Luo, K. Xiang, et al., Chem. Eng. J. 458 (2023) 141381.
[6] W. Deng, Y. Xu, X. Zhang, et al., J. Alloy. Compd. 903 (2022) 163824.
[7] T. Zhang, H. Sun, C. Yin, et al., Prog. Mater. Sci. 140 (2023) 101207.
[8] X. Wu, X. Chen, Q. Zhang, et al., Energy Storage Mater. 44 (2022) 29–47.
[9] D. Yue, J. Yin, W. Zhang, et al., Adv. Funct. Mater. 33 (2023) 2300658.
[10] Y. Liu, H. Luo, F. Wang, et al., J. Mater. Chem. C 11 (2023) 10985–10992.
[11] X. Li, Z. Shi, M. Han, et al., Mater. Today Energy 29 (2022) 101119.
[12] H. Li, L. Wang, Y. Zhu, et al., Chin. Chem. Lett. 32 (2021) 2229–2232.
[13] M. Guo, J. Jiang, Z. Shen, et al., Mater. Today 29 (2019) 49–67.
[14] J. Jiang, Z. Shen, J. Qian, et al., Energy Storage Mater. 18 (2019) 213–221.
[15] S. Zhang, T. Fu, Y. Gong, et al., Chin. Chem. Lett. 34 (2023) 107615.
[16] H. Luo, F. Wang, R. Guo, et al., Adv. Sci. 9 (2022) 202202438.
[17] Y. Wang, C. Xie, S. Luo, et al., ACS Appl. Energy Mater. 4 (2021) 6135–6145.
[18] J. Wang, Y. Xie, J. Liu, et al., Appl. Surf. Sci. 469 (2019) 437–445.
[19] J. Liu, M. Li, Y. Zhao, et al., J. Mater. Chem. A 7 (2019) 19407–19414.
[20] S. Luo, J. Yu, S. Yu, et al., Adv. Energy Mater. 9 (2019) 1803204.
[21] H. Luo, X. Zhou, C. Ellingford, et al., Chem. Soc. Rev. 48 (2019) 4424–4465.
[22] H. Li, T. Feng, Y. Liang, et al., Chin. Chem. Lett. 34 (2023) 108350.
[23] Y. Cheng, Z. Pan, H. Bai, et al., ACS Appl. Mater. Interfaces 14 (2022) 8448–8457.
[24] C. Tan, X. Cao, X. Wu, et al., Chem. Rev. 117 (2017) 6225–6331.
[25] S. Mohammad, S. Shingdilwar, S. Banerjee, et al., Prog. Poly. Sci. 106 (2020) 101255.
[26] S. Zhang, B. Zhang, J. Zhang, et al., ACS Appl. Mater. Interface 13 (2021) 32242–32250.
[27] B. Xie, J. Cai, T. Wang, et al., J. Inorg. Mater. 38 (2023) 137–147.
[28] J. Wang, Y. Xie, Y. Zhang, et al., Mater. Chem. Front. 5 (2021) 3646–3656.
[29] J. Wang, S. Liang, J. Xiong, et al., Compos Part A-Appl. Sci. 163 (2022) 107254.
[30] R. Liu, J. Zhao, Q. Han, et al., Adv. Mater. 30 (2018) 1802851.
[31] Y. Xie, W. Jiang, T. Fu, et al., ACS Appl. Mater. Interface 10 (2018) 29038–29047.
[32] Y. Xie, J. Wang, S. Tan, et al., ACS Appl. Energy Mater. 3 (2020) 7952–7963.
[33] Y. Zhang, C. Zhang, Y. Feng, et al., Nano Energy 56 (2019) 138–150.
[34] H. Zhang, M. Marwat, B. Xie, et al., ACS Appl. Mater. Interfaces 12 (2020) 1–37.
[35] Z. Liu, M. Meyers, Z. Zhang, et al., Prog. Mater. Sci. 88 (2017) 467–498.
[36] J. Wang, Y. Xie, C. Chen, et al., IET Nanodielectrics 4 (2021) 171–178.
[37] M. Zhang, B. Li, J. Wang, et al., Adv. Mater. 33 (2021) 2008198.
[38] Y. Jiang, X. Zhang, Z. Shen, et al., Adv. Funct. Mater. 30 (2020) 1906112.
[39] C. Wang, G. He, S. Chen, et al., J. Mater. Chem. A 9 (2021) 8674–8684.
[40] J. Wang, Y. Su, B. Wang, et al., Nano Energy 72 (2020) 104665.
[41] H. Kojima, Y. Otake, T. Takahashi, et al., IEEE T. Dielect. El. In. 23 (2016) 43–48.
[42] Q. Feng, Q. Dong, D. Zhang, et al., Compos. Sci. Technol. 218 (2022) 109193.
[43] Z. Xie, D. Liu, X. Tang, et al., Compos. Sci. Technol. 232 (2023) 109856.
[44] Y. Xie, J. Wang, Y. Yu, et al., Appl. Surf. Sci. 440 (2018) 1150–1158.
[45] J. Chen, J. Liu, L. Cai, et al., Compos. Sci. Technol. 200 (2020) 108381.
[46] J. Wang, Y. Xie, J. Liu, et al., Polymers 10 (2018) 1349.
[47] Z. Shen, J. Wang, J. Jiang, et al., Nat. Commun. 10 (2019) 1843.
[48] Z. Cai, X. Wang, L. Li, et al., Extreme Mech. Lett. 28 (2019) 87–95.
[49] W. Hong, K. Pitike, Proc. Iutam. 12 (2015) 73–82.
[50] Y. Wang, L. Wang, Q. Yuan, et al., J. Mater. Chem. A 5 (2017) 10849–10855.
[51] R. Anderson, IEEE Ind, Applic. Soc, 1996, pp. 1327–1330.
[52] J. Li, H. Gong, Q. Yang, et al., Appl. Phys. Lett. 104 (2014) 263901.
[53] Y. Xie, Y. Yu, Y. Feng, et al., ACS Appl. Mater. Interface 9 (2017) 2995–3005.
[54] X. Xiong, D. Shen, Q. Zhang, et al., Compos. Commun. 25 (2021) 100682.
[55] X. Wu, S. Tang, G. Song, et al., Nano Express 2 (2021) 010025.
[56] H. Jung, J. Kim, J. Lim, et al., Electron. Mater. Lett. 16 (2020) 47–54.
[57] J. Chen, Y. Wang, Q. Yuan, et al., Nano Energy 54 (2018) 288–296.
[58] H. Ye, F. Yang, Z. Pan, et al., Acta Mater. 203 (2021) 116484.
[59] X. Zhang, D. Hu, Z. Pan, et al., Chem. Eng. J. 406 (2021) 126818.